Fluorescence and bright-field 3D image fusion based on sinogram unification for optical projection tomography

Tang, X.; Hoff, V.M.; Hoogenboom, J.; Guo, Y.; Cai, F.; Lamers, G.; ... ; Wang, G.

Fluorescence and Bright-field 3D Image Fusion Based on Sinogram Unification for Optical Projection Tomography

Xiaoqin Tang, Merel van't Hoff, Jerry Hoogenboom, Yuanhao Guo, Fuyu Cai, Gerda Lamers, Fons Verbeek*
Leiden Institute of Advanced Computer Science, Leiden University
Niels Bohrweg 1, 2333CA Leiden, Netherlands
{x.tang, f.j.verbeek}@liacs.leidenuniv.nl, merelvanthoff@gmail.com

***Abstract*—In order to preserve sufficient fluorescence intensity and improve the quality of fluorescence images in optical projection tomography (OPT) imaging, a feasible acquisition solution is to temporally formalize the fluorescence and bright-field imaging procedure as two consecutive phases. To be specific, fluorescence images are acquired first, in a full axial-view revolution, followed by the bright-field images. Due to the mechanical drift, this approach, however, may suffer from a deviation of center of rotation (COR) for the two imaging phases, resulting in irregular 3D image fusion, with which gene or protein activity may be located inaccurately. In this paper, we address this problem and consider it into a framework based on sinogram unification so as to precisely fuse 3D images from different channels for CORs between channels that are not coincident or if COR is not in the center of sinogram. The former case corresponds to the COR deviation above; while the latter one correlates with COR alignment, without which artefacts will be introduced in the reconstructed results. After sinogram unification, inverse radon transform can be implemented on each channel to reconstruct the 3D image. The fusion results are acquired by mapping the 3D images from different channels into a common space. Experimental results indicate that the proposed framework gains excellent performance in 3D image fusion from different channels. For the COR alignment, a new automated method based on interest point detection and included in sinogram unification, is presented. It outperforms traditional COR alignment approaches in combination of effectiveness and computational complexity.**

Keywords—3D image fusion; sinogram unification; OPT; COR

I. INTRODUCTION

Understanding how genes coordinate the myriad of cellular processes involved in organogenesis remains one of the frontiers of modern science. However, experimental acquisition of the genetic information at the molecular level is still beyond our current capabilities. A viable alternative to gathering molecular-kinetic information about gene networks is to gather accurate and quantitative activity-state data including gene expression patterns and protein state distributions [1]. In this case, the ability to map gene and protein activity within 3D shaped organs plays an essential role in biological research, as knowledge of where genes are expressed gives us insight into their function, and the gene distribution gives us clues about which genes or proteins interact with each other [2, 3]. Consequently, a reliable 3D imaging technology to locate and digitize gene expressing patterns could therefore prove to be an essential complement and boost to more traditional biochemical approaches [4].

To image small animal organs and embryos measuring between 1mm and 1cm, in 2002 Sharpe et al proposed OPT to fill the size gap between confocal microscopy and magnetic resonance imaging (MRI) [5]. It allows for acquisition of high resolution full body images of animal organs with excellent spatial resolution and contrast and with minimal shadowing artifacts due to back-projection reconstruction after multi-angle projection acquisition [6, 7]. In OPT imaging, the first step is to apply a fluorescent labeling of gene and/or protein. Secondly, specimen is imaged in fluorescence and bright-field channels and reconstructed to a 3D volume. Finally, gene or protein can be localized by integrating the fluorescence 3D image into the bright-field 3D image [8]. In order to focus on the acquisition of high-quality OPT images in short time and retaining sufficient fluorescence intensity, we have developed an improved OPT imaging system wherein for a specimen all fluorescence images are acquired before bright-field images. In this case, with regard to 3D image reconstruction and fusion, not only COR position but also the accumulated mechanical drift between two phases should be considered.

When applying the inverse radon transform for 3D reconstruction, the COR position should be in the middle of the sinogram. This could be achieved by COR alignment, which was first studied in 1990 [9] in computational tomography (CT). Previous studies showed that misaligned COR could introduce severe artefacts or even incorrect results [10, 11]. Furthermore, in OPT it avoids the long time spent on hardware calibration before imaging, ameliorating the efficiency of the imaging system. Regarding COR alignment methodologies, there are two mainstream approaches: the first approach is based on signal match for pairs of projection data (180° opposed to each other) [9, 12, 13, 14]. They are widely used in CT because the projected intensities from two opposite angles are theoretically equivalent in this imaging system. Unfortunately, these methods may not be suitable for OPT images, as opposite projected data vary differently at different angles. These differences are caused by the fact that OPT only images the front half of the specimen [5]. Moreover, they are not feasible when the sinogram is disturbed by fixed defects or rand-

* Corresponding Author

978-1-5090-1610-5/16/$31.00 ©2016 IEEE

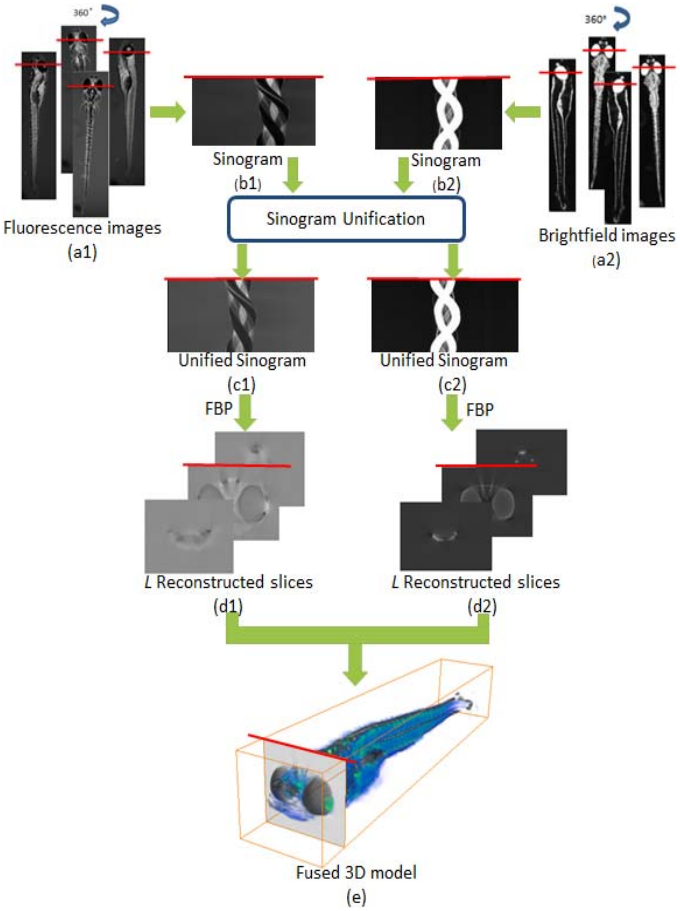

Fig. 1. Framework of fluorescence and bright-field 3D image fusion for OPT imaging. (a1), (b1), (c1), (d1) Images, sinogram, unified sinogram and reconstructed slices of 6 days post-fertilization (dpf) zebrafish in the fluorescence channel. (a2), (b2), (c2), (d2) The corresponding images, sinogram, unified sinogram and reconstructed slices in bright-field channel. Sinogram unification and 3D reconstruction are applied to both channels separately. (e) Fused 3D image. Fluorescence signals are shown from green to blue (strong to weak), and the bright-field signal is shown in gray. Images with a red line correspond to the same slice in the specimen.

om noise, which frequently occurs in OPT imaging. The second mainstream approach both for CT and OPT is based on iterative reconstruction in the sinogram [15, 16, 17]. The vertical axis producing the smallest variance in reconstructed image is chosen as the COR in [16]. However, this approach is time-consuming, making it seldom used in CT. Furthermore, both approaches choose only one sinogram for COR alignment, so the COR fluctuation produced by different sinograms is not taken into account, resulting in unconvincing COR.

Therefore we aim to locate convincing COR while achieving a significant decrease in the computational cost by presenting a new COR alignment methodology. Constrained by the OPT imaging mechanism, projection pairs from opposite angles are not all equivalent. We first detect the interest points where the neighboring projections are relatively equivalent with those of their opposite points. The distance between neighboring projections of interest points and those of their opposite points reaches the minimum when the COR is most close to the ideal value. With this hypothesis, the COR could be located in the sinogram. To make the COR convincing, multiple sinograms are considered, which are detected automatically from the OPT images, based on the range where signals exist. Traditionally, images in different channels are regarded to share the same COR; therefore 3D images from different channels are reconstructed and fused based on the single-channel located COR.

In this paper we propose an improved framework of 3D image reconstruction and fusion by taking the mechanical drift into account for our improved OPT system. In this framework depicted in Fig.1, sinogram unification including COR alignment and sinogram resizing, is introduced before 3D reconstruction for each channel. As stated above, COR alignment is related to rectifying shift between COR position and center of sinogram. Thus sinogram resizing is responsible for correcting mechanical drift between two channels, guaranteeing that each pair of reconstructed voxels is registered to the same voxel in the fused 3D image. Moreover, sinogram unification avoids the time spent on adjusting the rotation axis to the middle of Field of View (FOV) before imaging process. With the correct 3D fusion result, accurately locating and digitizing gene or protein activity becomes possible.

II. Fluorescence and Bright-field 3D Image Fusion

A. OPT images from the improved OPT imaging system

The images from our OPT system come with improved sample preparation and image acquisition. For each specimen, the fluorescence images were acquired before the bright-field images. Improved sample preparation included counterstain optimizing, agarose embedding and optical clearing. Different solutions were analyzed and compared quantitatively to optimize the sample preparation, with which more high-quality images were imaged in a given period of time. Optimization of image acquisition involved calibration of microscope, decrease of imaging artefacts and optimization of gain. Importantly, several influences on image quality including mechanical drift in the stepper motor, heat generation, dissolution of the glue and agarose shrinkage, were considered and optimized to decrease the artefacts produced in the imaging process. Some image samples are shown in Fig. 1 (a1) and (a2). The raw data of a specimen for each channel is a 16-bit high-resolution image of size 1036×1360×400 pixels, with a file size of 1.05GB. 1036×1360 is the image size for one angle, and 400 is the number of rotation angles in [0°, 360°). In most cases presented here, Green Fluorescent Protein (GFP) was used as fluorescence signal for imaging. As images from different channels were acquired at different times, the corresponding 3D images after 3D reconstruction should not be directly fused without considering possible mechanical drift from the rotation.

B. Sinogram unification

Sinogram unification is defined to unify sinograms in different channels before 3D reconstruction under the condition that the detector and rotation stage is not tilted, so that each pair of reconstructed voxels is registered to the same voxel in the fused 3D image with minimum reconstruction artefacts. It includes the automatic processes of COR alignment and sinogram resizing.

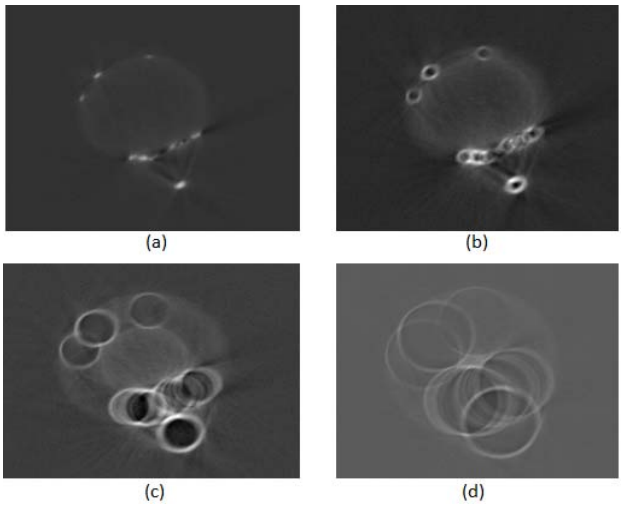

Fig. 2. (a) One slice of the reconstructed bright-field images of 3 dpf zebrafish embryo without COR shift. (b) The reconstructed slice with a shift of 5 pixels between COR and sinogram centre, showing the artefacts. (c) and (d) The results with a shift of 20 pixels and 52 pixels, respectively.

1) COR alignment: Considering the artefact effect of COR shift on reconstructed images as shown in Fig. 2 (b, c, d), a novel COR alignment approach is presented to solve the computationally expensive problem and to refine the unconvincing result from only one sinogram in [16].

According to the principle of OPT imaging, only the front half of specimen is in focus, so the projected data from opposite angles may vary differently depending on the rotation angle, specimen size and shape. However, for a voxel at the left or right boundary of the specimen, the opposite projected data are equivalent. This equivalence is shown as a peak and trough in the sinogram edge. To illustrate our hypothesis, a sinogram of the fluorescent channel of zebrafish larva is depicted as an example in Fig. 3. Point O, A and B are the fluorescence signals of 6 dpf zebrafish eye from 3 different angles, and O*, A* and B* are their corresponding opposite projections. The projected data for an eye voxel should be formed as a sine function passing through O, A, B, O*, A* and B* in CT system, but in OPT only O and O* remain equivalent; while A and A* as well as B and B* differ significantly, being consistent with the hypothesis above. With this hypothesis, the COR could be located with the oppositely projected pairs that are similar to O and O*. The problem of locating the COR is therefore transformed as search for peaks and troughs in the sinogram edge, in our case defined as interest points.

a) Interest point detection: A sinogram is defined as $S(\xi, \varphi)$ with a size of $400 \times p$, where φ is the rotating angle, and ξ is the phase in each angle. As described in Algorithm 1, the procedure of interest point detection is based on point selection with initial points $E = \{\xi_k, \varphi_k\},\ k \in [1, M]$, the collection of points using edge detection in sinogram. M is the number of initial points. After point selection, the detected interest points interest points are $P = \{\xi_j, \varphi_j\},\ j \in [1, N]$, and $N \leq M$. The specific steps of point selection are depicted in Algorithm 1, and the size of both patch $W0_k$ and W_k are w_1.

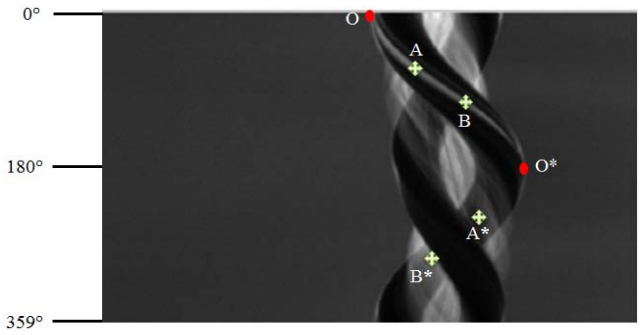

Fig. 3. The sinogram in Fig. 1 (b1), showing the differences among pairs of opposite projected data. O and O*, A and A*, B and B* are pairs respectively. O and O* are interest points; while A and A*, B and B* are not.

Algorithm 1: Interest Point Detection in sinogram

Input: $S(\xi, \varphi), E = \{(\xi_k, \varphi_k)\},\ k \in [1, M]$
Binarize sinogram $S(\xi, \varphi)$
for each initial point (ξ_k, φ_k) in binarized sinogram **do**
  Creat patch $W0_k$ of size w_1 centered by (ξ_k, φ_k) and update it as W_k with only one 1-labeled region remaining
  Detect the new edge ED_k in the binary patch W_k
  if the edge ED_k is not enclosed **then**
    if $\tan\theta < \frac{\sqrt{3}}{3}$, θ is the angle passing through 0-labeled centre $(\xi_{zero}, \varphi_{zero})$ and 1-labeled centre $(\xi_{one}, \varphi_{one})$ in W_k **then**
      if (ξ_k, φ_k) is peak or trough as defined in *Eq*(1) **then**
        (ξ_k, φ_k) is remained as one of the interest points $P = \{(\xi_j, \varphi_j)\},\ j \in [1, N]$
      else if (ξ_k, φ_k) meet the *Eq*(2) or *Eq*(3) **then**
        increase the size of $W0_k$ and do the **for** loop again
      end if
    end if
  end if
end if
end for

Constrained by $\tan\theta < \frac{\sqrt{3}}{3}$ in Algorithm 1, only points with $\theta < 30°$ are remained. We define θ as the angle passing through the 0-labeled center $(\xi_{\text{zero}}, \varphi_{\text{zero}})$ and the 1-labeled center $(\xi_{one}, \varphi_{one})$ that are separated by edge ED_k in its patch W_k, instead of defining θ as the slope of ED_k. The peak and trough within W_k (red stars in Fig. 4) are defined as following:

$$\text{Peak:}\begin{cases} \xi_{zero} > \xi_{one} \\ |D_\varphi| = (w_1 - 1) \\ D(D_\xi) < 0 \\ 1 \notin sign(d_{\xi_1}) \\ 1 \notin sign(d_{\xi_2}) \end{cases} \quad \text{Trough:}\begin{cases} \xi_{zero} < \xi_{one} \\ |D_\varphi| = (w_1 - 1) \\ D(D_\xi) > 0 \\ -1 \notin sign(d_{\xi_1}) \\ -1 \notin sign(d_{\xi_2}) \end{cases} \quad (1)$$

D_φ symbolizes the sum of derivatives of ED_k in the φ direction along the edge curve, while $D(D_\xi)$ is the sum of second derivatives of ED_k in the ξ direction along the edge curve. When $D(D_\xi) < 0$, the function of ED_k sequence is constrained as convex, and if $D(D_\xi) > 0$, it is concave, corresponding to the peak and trough, respectively. We break ED_k into upper and lower edges: ED_{k1} and ED_{k2}, both of which are started at the middle of ED_k in the φ direction. $d_{\xi 1}$ and $d_{\xi 2}$ are the derivatives of ED_{k1} and ED_{k2} separately in the ξ direction.

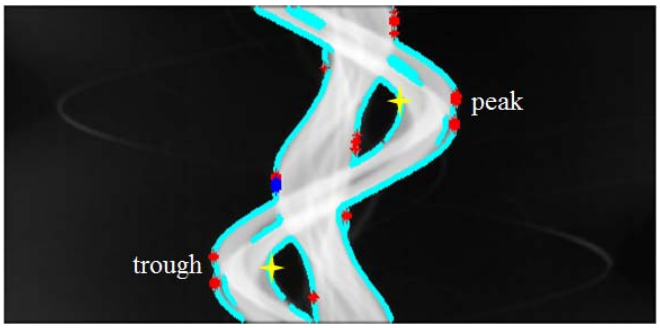

Fig. 4. Bright-field sinogram from 5 dpf chicken embryo heart images with interest points detected (shown as red and blue stars). Edge points (initial points) are shown as cyan points; while false-peak are shown as yellow cross.

With the definition in Eq. (1), false-peak and false-trough (yellow crosses in Fig. 4) are not kept as interest points, as they are not true sine peaks but rather intersections of different sine functions, which should be discarded. Furthermore, when a true trough satisfies Eq. (2) (blue star in Fig. 4):

$$\begin{cases} \xi_{zero} < \xi_{one} \\ |D_\varphi| = (w_1 - 1) \\ D(D_\xi) = 0 \\ sign(d_{\xi 1}) = 0 \\ sign(d_{\xi 2}) = 0 \end{cases} \tag{2}$$

or a true peak satisfies Eq. (3):

$$\begin{cases} \xi_{zero} > \xi_{one} \\ |D_\varphi| = (w_1 - 1) \\ D(D_\xi) = 0 \\ sign(d_{\xi 1}) = 0 \\ sign(d_{\xi 2}) = 0 \end{cases}, \tag{3}$$

it means that edge ED_k in W_k of size w_1 is strictly vertical, so it does not satisfy the definition of peak or trough in Eq. (1). The reason for the inconsistency comes from the size of W_k. To solve this problem, a bigger patch (set as $2w_1$-1 in our experiment) should be set to satisfy Eq. (1) in a bigger patch, following the same steps in Algorithm 1.

b) COR alignment: With the interest points detected in a sinogram, the COR range is abtained as $[\xi_{min}, \xi_{max}]$, where ξ_{max} and ξ_{min} are the maximum and minimum of ξ_j in the interest points P. For a specific COR c, we locate the corresponding opposite points $P_c' = \{(\xi_j, \varphi_j)_c'\}$, $j \in [1, N]$ for all interest points P, which are symmetric by c and have an interval of 180° in projection. To find a mathematical metric between P and P_c', we define the neighbors of (ξ_j, φ_j) and $(\xi_j, \varphi_j)_c'$ as $r_c(\xi_j, \varphi_j)$ and $r_c'(\xi_j, \varphi_j)$. As shown in Fig. 3, the projection data betweem interest point (ξ_j, φ_j) and its opposite point $(\xi_j, \varphi_j)_c'$ should be equivalent, so we search for the optimal COR for the ith sinogram in the range $[\xi_{min}, \xi_{max}]$ by formulationg Eq. (4):

$$C_i^* = \min_c \frac{1}{N} \sum_j^N (r_c(\xi_j, \varphi_j) - r_c'(\xi_j, \varphi_j)) \tag{4}$$

The sinogram range S used for COR alignment, is obtained by choosing the smallest one among four ranges where fluorescence or bright-field signals exist in each of the four orthogonally projected raw OPT images (0°, 90°, 180°, and 270°). The range for each raw OPT image is roughly calculated by applying threshold segmentation based on the OTSU algorithm [18] to abstract the signals from the background. To reduce the redundancy of computation in COR alignement, s sinograms are selected from the range S by using a variable *step*. For the s sinograms, the corresponding optimal COR sequence is generated as $C = \{C_1^*, C_2^*, \dots, C_s^*\}$ using Eq. (4). The most frequently occurring value r in C is referred to as the optimal COR for 3D reconstruction. Sinogram S_i sized by $400 \times p$ could be aligned centered by r in the ξ direction, to S_i' of size $400 \times q$ by applying Eq. (5):

$$q = \begin{cases} 2 \times r, & r < \frac{p}{2} \\ 2 \times (p - r), & r \geq \frac{p}{2} \end{cases} \tag{5}$$

As illustrated in Eq. (5), q is calculated to be smaller than p to preserve sufficient sinogram information, as well as to avoid redundant background reconstruction, i.e. S_i is truncated as S_i' using Eq. (6), instead of extending it, which consumes more time in reconstructing the background.

$$S_i' = \begin{cases} S_i(1{:}\,2r, \varphi), & r < \frac{p}{2} \\ S_i(2r - p{:}\,p, \varphi), & r \geq \frac{p}{2} \end{cases} \tag{6}$$

2) Sinogram resizing: As in our OPT imaging system fluorescence images are acquired before bright-field images, the COR may deviate from the original position after a full rotation, owing to the inevitable mechanical drift. Consequently, the located CORs for both channels may suffer by tiny difference (0-2pixels in our experiment). The ith sinograms in the fluorescence and bright-field channels are obtained as S_{fi} sized by $400 \times p_f$ and S_{bi} sized by $400 \times p_b$. The aligned sinograms are S_{fi}' and S_{bi}', with size of $400 \times q_f$ and $400 \times q_b$respectively. To fuse the corresponding 3D images from both channels, S_{fi}' and S_{bi}' are resized as:

$$\begin{cases} S_{fi}^* = (z_0, S_{fi}', z_0);\ S_{bi}^* = S_{bi}', & q_f < q_b \\ S_{fi}^* = S_{fi}';\ S_{bi}^* = (z_0, S_{bi}', z_0), & q_f > q_b \end{cases} \tag{7}$$

Where z_0 is a zero matrix with size of $400 \times |r_f - r_b|$. r_f and r_b represent the located CORs for the fluorescence and bright-field sinograms. After resizing, S_{fi}^* and S_{bi}^* form a pair of sinograms for 3D reconstruction, so that the voxel pair in the reconstructed images of R_{fi} and R_{bi} could be registered to the same voxel in 3D space.

C. 3D image fusion

By applying FBP algorithm in fluorescence and bright-field channel, the reconstructed 3D images from L sinograms are formed as $R_f = \{R_{f1}, R_{f2}, \dots, R_{fl}, \dots, R_{fL}\}$ and $R_b = \{R_{b1}, R_{b2}, \dots, R_{bl}, \dots, R_{bL}\}$. The intensities in R_{fl} and R_{bl} refer to the fluorescence and bright-field signals. For transparent specimen such as zebrafish larvae in our experiment, the bright-field signals are generally distributed in vertebral and bones, describing the zebrafish silhouette. Therefore, by fusing R_f and R_b, fluorescence signals could be better located

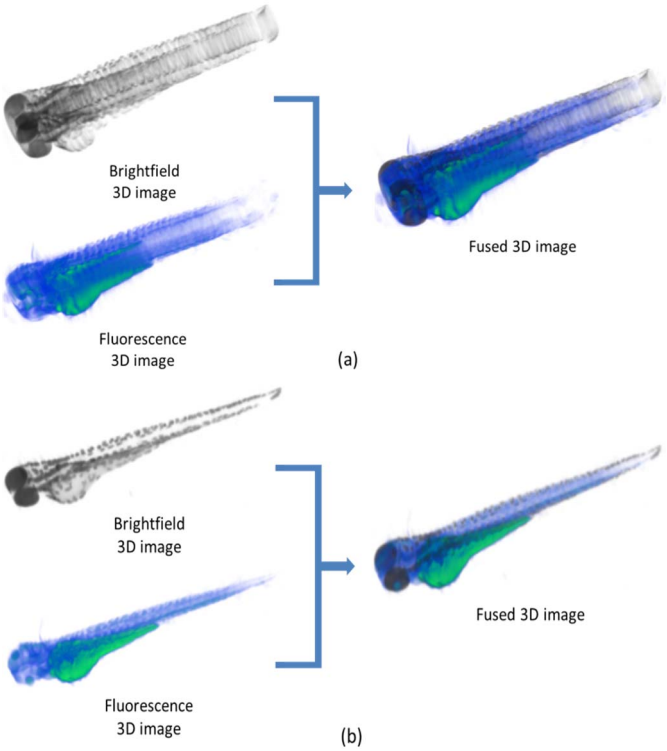

Fig. 5. 3D image comparison of 3 dpf zebrafish models. (a) Reconstructed 3D images without sinogram unification. (b) Reconstructed 3D images with sinogram unification. Bright-field signals are shown in gray, and fluorescence signals are shown in green and blue (green indicates strong fluorescence signal; while blue shows weak fluorescence signal).

and analyzed within specimens. R_f and R_b are fused according to their equivalent slice number l. For each voxel in the fused 3D image, $V_{(x,y,l)} = (I_f, I_b)$ describes its signals in different channels, and (x, y, l) symbolizes the coordinate in 3D space. (x, y) and l correspond to the pixel and the slice number of the reconstructed image. $V_{(x,y,l)}$ could be further used for 3D segmentation and quantitative calculation of fluorescence labeling (gene and/or protein activity) in specimen or organs.

III. Experimental Results

A. Reconstructed 3D image comparison

The reconstructed 3D images with and without sinogram unification are shown in Fig. 5. The experiments are implemented on the 3 dpf zebrafish. The size of sinograms S_i for both channels are 400×1036 pixels. The fused 3D image without sinogram unification is shown as Fig. 5 (a), which suffers from severe artefacts around the specimen in both channels, as well as dislocation between them. Conversely, the results with sinogram unification in Fig. 5 (b) describe clear and distinct signals in both channels. Vertically in sinograms, the located CORs for the fluorescence and bright-field channels are 569 and 570, with 1 pixel of deviation after a full rotation of 360°. More fused 3D image comparisons, including the HH36 chicken embyo heart and the 6 dpf zebrafish brain, can be found in Fig. A1. On the two datasets, COR disparities between channels are 1 pixel (located at 525 and 526) and 2 pixels (located at 261 and 263), respectively. By fusing 3D images after sinogram unification and 3D reconstruction, fluorescence signals can be accurately visualized and located within the specimen.

In this section, the reconstructed results with and without sinogram unification are compared quantitatively on the same dataset as in Fig. 5. Inspired by [16], we analyzed the variance of the reconstructed image slices because reconstructed image with smaller variance indicates more blur and similarities, which is consistent with the artefacts produced by misaligned COR. The variances of all reconstructed slices are shown in Fig. 6 (a) and (b). Obviously, for both channels employing sinogram unification gains larger variances, introducing less blurred artefacts. What should be noted is that there are no evident variance differences on both sides of Fig. 6 (a) and (b), because no fluorescence or bright-field signal occurs on both sides, producing approximately equivalent variances approaching to 0. (b), (c), (e), (f) are the comparison of one reconstructed slice (slice 940). (g), (h) show the fused comparison without and with sinogram unification (slice 940 to 949). Noting the top edge of (g), we see a dislocation between channels; but in (h) no dislocation exists. Therefore, we conclude that with sinogram unification, not only the 3D images in both channels describe sharp fluorescence and bright-field information, but also they are integrated without dislocation.

B. Comparison of different COR alignment methods on OPT images

Three previous COR alignment approaches are analyzed and compared to our method on the OPT images of a 3 dpf zebrafish. The Pixel Match method [13] and the Cross Correlation Operation (CCO) method [14] are based on signal match for pairs of projection, both of which are successfully used in CT COR alignment. The most commonly used method in OPT COR alignment is the one proposed in [16], named as Automatic method in this paper. The results of [13], [14] and [16] strongly depend on the selection of sinograms. In order to produce convincing results, comparisons of different COR alignment methods are implemented on multiple sinograms selected with the proposed strategy above.

According to the explanation in Fig. 6, sinograms without fluorescence or bright-field signals make no contribution to COR alignment. Therefore, in our experiment the sinogam range S used for COR alignment is determined by locating where fluorescence or bright-field signals exist in raw OPT images as depicted above. To reduce the redundancy of computation, sinograms are selected by a step that varies according to the number of sinograms in S, referred as NS. Specifically, $NS \in [1,400]$, $NS \in (400,800]$ and $NS \in (800,1360]$ correspond to the step of 10, 20 and 30 respectively. From $s = NS/step$ sinograms, the obtained different CORs and their frequencies are shown in different colors and rectangle widths as shown in Fig. 7. Large rectangle width in Fig. 7 (a) implies high frequency. CORs from four methods are located at 513, 518, 515 and 516 in the fluorescence channel. For the bright-field images in Fig. 7 (c), the corresponding results are 516, 518, 517 and 517 respectively. Sinograms are unified and reconstructed based on the located CORs. The variances of the

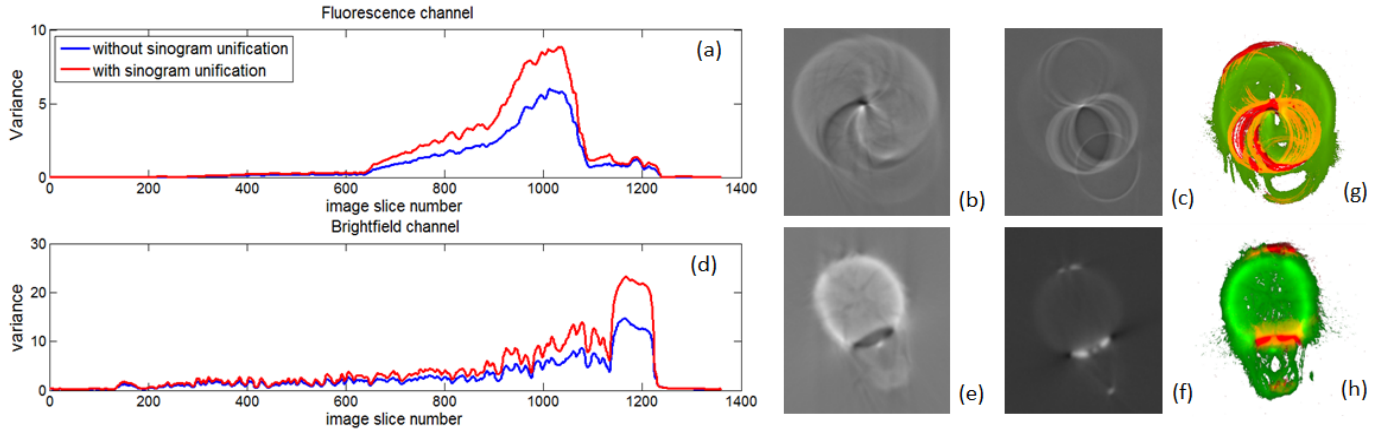

Fig. 6. Comparison of reconstructed image slices without and with sinogram unification. (a) , (d) The comparison of reconstructed image variances in the fluorescence and bright-field channel. (b), (c) One reconstructed image (slice 940) without sinogram unification in two channels. (e), (f) The same slice of reconstructed image with sinogram unification in two channels. (g), (h) Fused reconstructed slices (slice 940 to 949) without and with sinogram unification. Fluorescence and bright-field signals are shown in green and red, and the interation between two channels is shown in yellow. There is a dislocation between channels in (g), which is observed in the top edge of (g); while (h) intergrates both channels precisely.

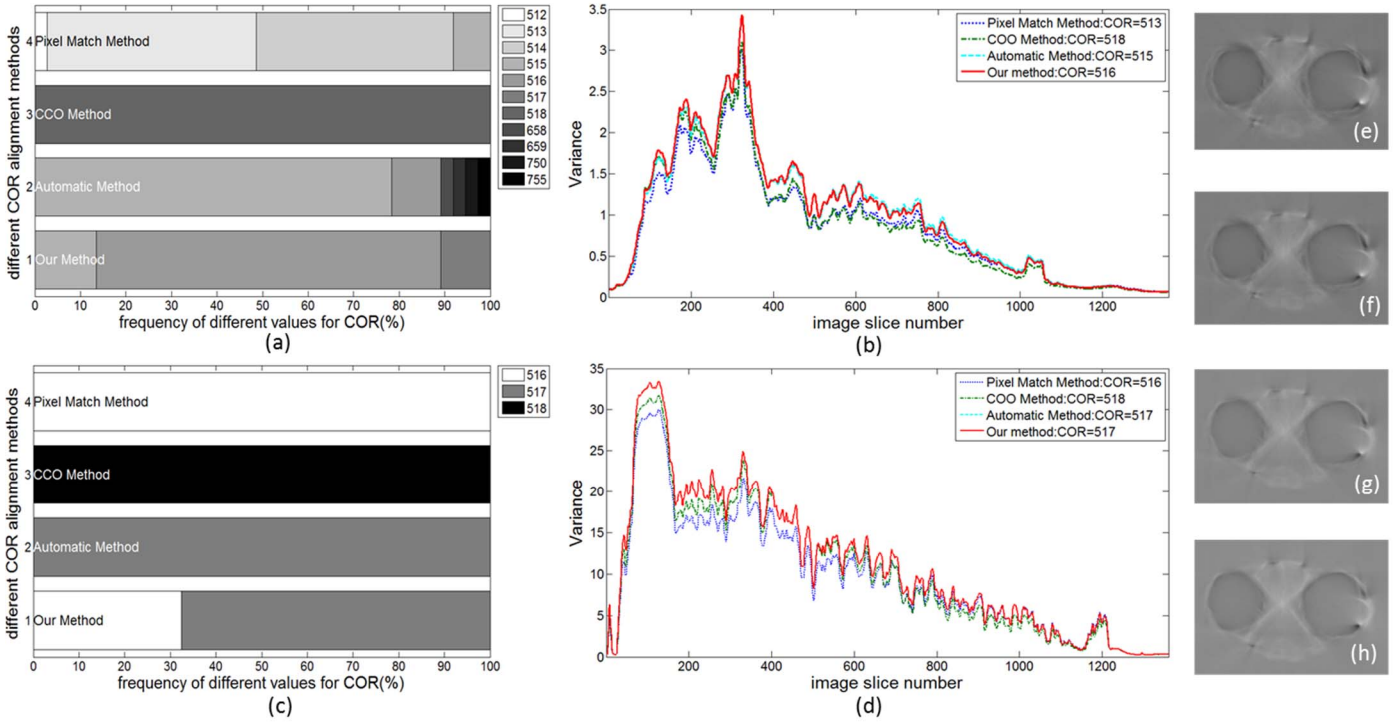

Fig. 7. COR and reconstruction comparison from different COR alignment methods. (a) and (c) Different COR values and their frequencies in the fluorescence and bright-field channels. The colors correspond to COR values, and the rectangle widths represent their frequencies. (b) and (d) Variances of all reconstructed slices in the fluorescence and bright-field channels with CORs from different methods. In (d) Variances of Automatic method and our method overlap, because CORs for both methods are equal as 517. (e)-(h) The same reconstructed slice (slice 100) by Pixel Match method, COO method, Automatic method and our method repectively.

reconstructed image are shown in (b) and (d). In the fluorescence channel (b), our method outperforms the other three methods with the largest overall variance, coinciding with the reconstructed results in (e)-(h) where the sharpness increases from (e) to (h). Not only in the fluorescence channel, but also in the bright-field channel the proposed method achieves the largest variance of all reconstructed slices.

To further verify the performance, experiments are implemented on 12 other datasets including zebrafish embryo (ZE), chicken embryo heart (CEH) and zebra finch embryo (ZFB) in the fluorescence (F) and bright-field (B) channel. From the results in Fig. 8, the Automatic method and our method obtained maximum variances on all the 12 datasets, because both methods achieved the optimal and equivalent

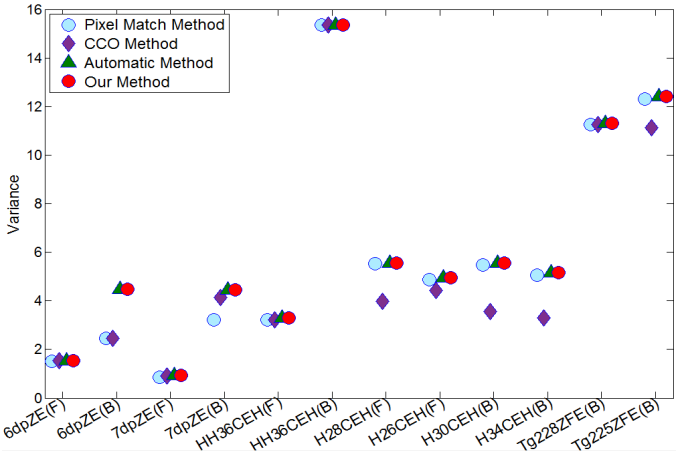

Fig. 8. Average Variances of reconstructed images with four COR alignment methods on 12 datasets. For each dataset, larger variance corresponds to less artefacts introduced by COR alignment. ZE is short for zebrafish embryo; CEH is for chicken embryo heart; ZFE represents zebra finch embryo; Different prefixes refer to different stages when specimens are imaged.

TABLE 1. RUNTIME of different COR alignment aprroaches in each sinogram on different datasets

Datasets	**Pixel Match**(s)	**CCO**(s)	**Automatic**(s)	**Ours**(s)
6dpf ZE (F)	0.6897	102.8966	1043.1034	10.3448
6dpf ZE (B)	0.6765	102.7941	1042.7941	12.2941
7dpf ZE (F)	0.6897	102.9310	1043.3793	11.7241
7dpf ZE (B)	0.6786	102.8929	1042.8214	11.7241
HH36 CEH (F)	0.6774	102.9032	1043.2580	2.2258
HH36 CEH (B)	0.6667	102.9333	1042.8444	6.2888
H28 CEH (F)	0.6800	103.1200	1043.1200	5.2000
H26 CEH (F)	0.7200	103.2000	1043.2000	4.3200
H30 CEH (B)	0.6774	103.5484	1043.1935	4.1612
H34 CEH (B)	0.6897	103.5517	1043.0344	3.3793
Tg228 ZFE (B)	0.7143	103.1786	1042.8571	2.6785
Tg225 ZFE (B)	0.7857	103.2143	1042.7857	2.7857
Average	**0.6955**	**103.097**	**1043.0326**	**6.4272**

COR on each dataset. The Pixel Match and CCO methods gained lower variances, resulting in more artefacts in reconstructed images.

Apart from the competitive effectiveness to the Automatic method in Fig. 8, our method performs significantly superior to CCO method and Automatic method in terms of its computational complexity; cf. Table 1. With the computer configuration of 16Gb RAM and 8-core 3.4GHz CPU, the average runtime for different COR alignment methods on one sinogram are 0.6955s, 103.097s, 1043.0326s and 6.4272s respectively. The pixel Match method achieves highest performance in runtime, but its capability of optimal COR alignment is frustrating. Overall, our method outperforms the other three in the combination of effectiveness and computational complexity. It is noteworthy that in our method the runtime on each dataset varies due to the differences in the number of interest points; while other three approaches consume approximately the same fixed runtime for each sinogram.

IV. CONCLUSION

The focus of this paper is to present a framework based on sinogram unification for 3D image fusion in different channels for OPT images, as well as a new automatic COR alignment method that outperforms other COR alignment approaches in general efficiency. Furthermore, the new COR alignment methodology could suppress random and fixed machine noise in background from OPT imaging system, because only peaks and troughs from foreground are detected in the sinogram as interest points. Importantly, the proposed framework and COR alignment are also suitable for 3D CT image fusion and comparison when tracking medical therapy, as well as multi-channel 3D image fusion in OPT. All the Experiments in this paper were implemented on a personal computer with an i7 processor and 16Gb RAM. Currently, the integrated system including imaging, sinogram unification, 3D reconstruction, 3D image fusion and visualization is being constructed as a distributed application on a cluster. With this integrated system, signals in different channels for the specimens can be imaged and visualized in 3D space within a very short period of time. Moreover, a quantitative 3D model for locating and calculating fluorescence signals (gene and/or protein activity) within specimen will be established in our future work.

V. ACKNOWLEDGMENT

The work is partially funded by China Scholarship Council (CSC).

REFERENCES

[1] Sharpe J. Optical projection tomography. Annu. Rev. Biomed. Eng., 2004, 6: 209-228.

[2] Maddox J. Is molecular biology yet a science? Nature, 1992, 355-201.

[3] Reinitz J, Sharp DH. Mechanism of eve stripe formation. Mech,Dev,1995. 49:33-58.

[4] Welten M C M. Spatio-temporal gene expression analysis from 3D in situ hybridization images. Leiden Institute of Advanced Computer Science, group Imaging and Bio-informatics, Faculty of Science, Leiden University, 2007.

[5] Sharpe J, Ahlgren U, Perry P, et al. Optical projection tomography as a tool for 3D microscopy and gene expression studies. Science, 2002, 296(5567): 541-545.

[6] Michálek J, Čapek M. Artifact-free 3D Reconstruction for Optical Projection Tomography. Microscopy and Microanalysis, 2014, 20(S3): 1362-1363.

[7] Singh M, Nair A, Vadakkan T, et al. Comparison of optical projection tomography and optical coherence tomography for assessment of murine embryonic development//SPIE BiOS. International Society for Optics and Photonics, 2015: 93340J-93340J-8.

[8] Correia T, Lockwood N, Kumar S, et al. Accelerated Optical Projection Tomography Applied to In Vivo Imaging of Zebrafish[J]. PloS one, 2015, 10(8): e0136213.

[9] Azevedo S G, Schneberk D J, Fitch J P, et al. Calculation of the rotational centers in computed tomography sinograms. IEEE transactions on nuclear science, 1990, 37(4): 1525-1540.

[10] Quanhong Z. Optimization research on X-ray industrial CT imaging. Beijing: Beijing University of Aeronautics and Astronautics; 2005. In Chinese.

[11] Zitova B, Flusser J. Image registration methods: a survey. Image and vision computing, 2003, 21(11): 977-1000.

[12] Olander B. Center of rotation determination using projection data in x-ray micro computed tomography. Sweden: Linkoping University; 1994.

[13] Kratochvila B J. 3D Computed Tomography. Czech: Czech Technical University in Prague; 2008.

[14] Min Y, Haidong C, Xingdong L, Fanyong M, Dongbo W. A new method to determine the center of rotation shift in 2D-CT scanning system using image cross correlation. NDT&E Int 2012;46:48-54.

[15] Brunetti A, De Carlo F. A robust procedure for determination of center of rotation in tomography//Optical Science and Technology, the SPIE 49th Annual Meeting. International Society for Optics and Photonics, 2004: 652-659.

[16] Donath T, Beckmann F, Schreyer A. Automated determination of the center of rotation in tomography data. JOSA A, 2006, 23(5): 1048-1057.

[17] Walls J R, Sled J G, Sharpe J, et al. Correction of artefacts in optical projection tomography. Physics in medicine and biology, 2005, 50(19): 4645.

[18] Otsu N."A Threshold Selection Method from Gray-Level Histograms," IEEE Transactions on Systems, Man, and Cybernetics, Vol.9, No.1, pp.62-66,1979.

Appendix

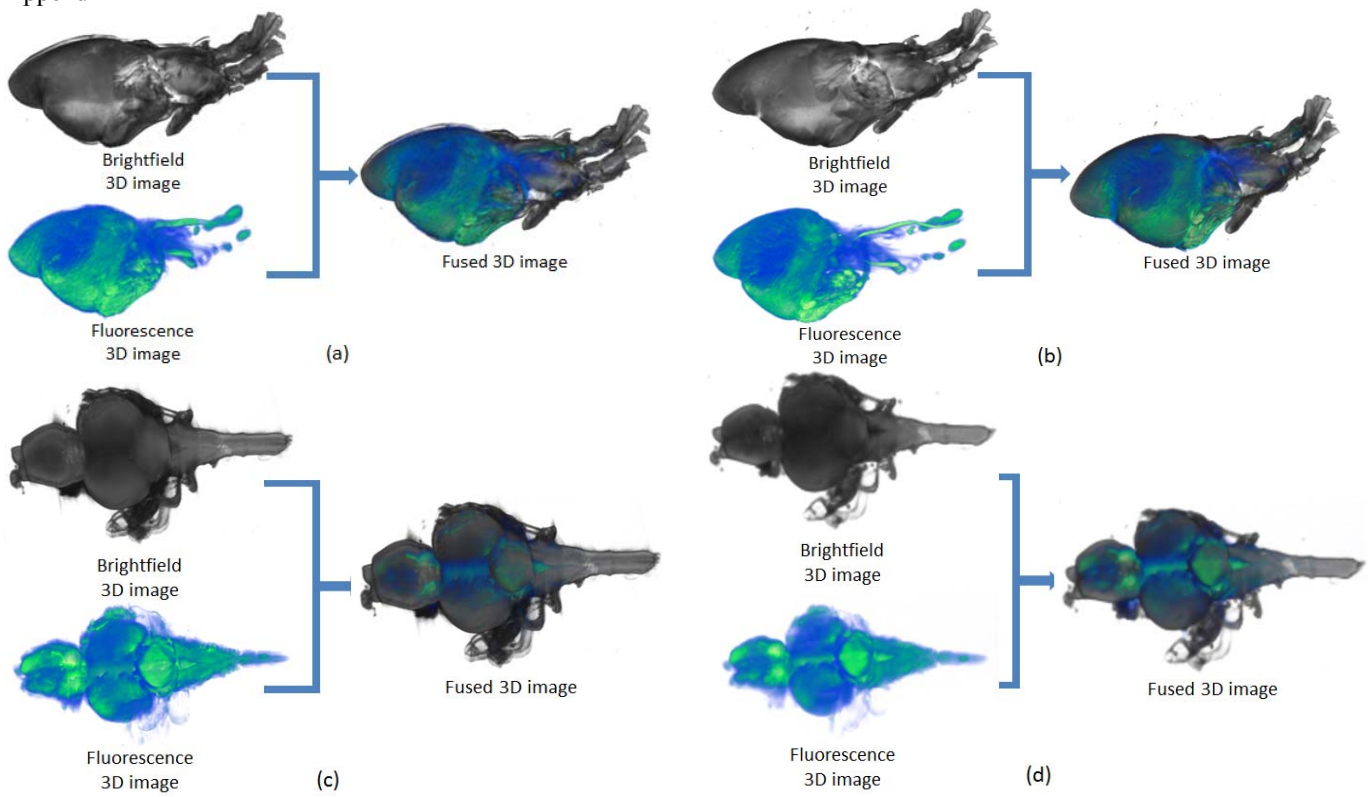

Fig. A1. Fused 3D image comparisons without and with sinogram unification in different dataset samples. Left (a,c) shows the results without sinogram unification. Right (b,d) indicates the 3D images with sinogram unification. (a) and (b) The HH36 chicken embyo heart. CORs are located at 525 and 526 in fluorescence and bright-field channel, with a disparity of 1pixel. (c) and (d) The 6 dpf zebrafish brain. CORs are located at 261 and 263 suffering a disparity of 2 pixels.